# Health Monitoring of Composite Plates using Acoustic Wave Propagation, Continuous Sensors and Wavelet Analysis

A. GHOSHAL*
*United Technologies Research Center, East Hartford, CT 06108, USA*

W. N. MARTIN
*Naval Undersea Warfare Center, Newport, RI 02841, USA*

M. J. SCHULZ
*Dept. of Mechanical Engineering, University of Cincinnati, OH 45221, USA*

A. CHATTOPADHYAY
*Dept. of Mechanical Engineering and Aerospace Engineering*
*Arizona State University, Tempe, AZ 85287, USA*

W. H. PROSSER
*NASA Langley Research Center, Hampton, VA 23681, USA*

H. S. KIM
*Inha University, Incheon, South Korea*

**ABSTRACT:** Health monitoring of aerospace structures can be done passively by listening for acoustic waves generated by cracks, impact damage and delaminations, or actively by propagating diagnostic stress waves and interpreting the parameters that characterize the wave travel. This paper investigates modeling of flexural wave propagation in a plate and the design of sensors to detect damage in plates based on stress wave parameters. To increase understanding of the actual physical process of wave propagation, a simple model is developed to simulate wave propagation in a plate with boundaries. The waves can be simulated by applied forces and moments in the model either to represent passive damage growth or active wave generation using piezoceramic actuators. For active wave generation, the model considers a piezoceramic patch bonded perfectly to a quasi–isotropic glass–epoxy composite plate. Distributed sensors are used on the plate and are modeled as being constructed using active fiber composite and piezoceramic materials. For active wave generation, a moment impulse is generated by the actuation of a piezoceramic patch. The waves generated from the patch are detected by the distributed sensor. For passive sensing of acoustic waves, a step function is used to simulate an acoustic emission from a propagating damage. The resulting acoustic wave is measured by the distributed sensor and produces micro-strains in the sensor nodes. The strains produce a single voltage signal output from the distributed sensor. Computational simulations and animations of acoustic wave propagation in a plate are discussed in the article. A new method to locate the source of an acoustic emission using the time

*Author to whom correspondence should be addressed. E-mail: anindo_ghoshal@yahoo.com



0731-6844/07/01 0095–18 $10.00/0 DOI: 10.1177/0731684407069965

history of the dominant lower frequency components of the flexural wave mode detected by continuous sensors is also presented.

**KEY WORDS:** health monitoring, active wave propagation, distributed sensor.

## INTRODUCTION

ACTIVE PROPAGATION OF Lamb waves in the plane of the material is an emerging technique used to detect damage [1–7] in aerospace structures. Methods of measuring acoustic emissions (AE) are also used for damage detection [9–11]. The modeling of wave propagation is often done for plates that are of infinite dimension [13–18,27] because closed-form solutions of wave propagation in a bounded medium are difficult to obtain. A normal mode approach for obtaining a closed form solution for bending wave propagation in a plate is presented in References [19–22]. Finite-element methods are also used to model wave propagation, but the computation time is usually large and the representation of higher frequencies and modes are constrained by the number of elements used. Modeling of piezoceramic (PZT) actuators bonded to structures is given in References [23–26].

The normal mode approach is also used in the present paper to model asymmetric Lamb wave or flexural wave propagation in a simply supported plate. Much work had been performed that suggests cracks generate predominantly extensional mode AE signals and flexural modes AE signals to a less extent. Out-of-plane source-like impact damage or delaminations generate large flexural modes. Cracks not located at the midplane of a plate will also generate flexural modes but those near the midplane will not generate flexural modes. Hence the present model is mainly concerned with flexural mode AE signals from impact damage, delaminations and cracks not located at the mid-plane. A glass–epoxy composite plate is modeled here as quasi-isotropic, and piezoceramic actuators and sensors are modeled on the plate for generating and receiving the waves. The objective of developing this model is to provide a tool to simulate wave propagation and to facilitate the design of sensors to measure the waves. The model uses a closed-form solution and it is written in matrix and vector forms to run efficiently on a personal computer (PC). With this technique, series and array configurations of sensors can be investigated including different shapes of sensors and actuators. Piezoelectric patches are used as the sensor and actuator material. The sensor design can mimic receptors that excite dendrites that are the inputs of neurons in the human nervous system. Ten or more nodes can be connected in a continuous single channel nerve. This continuous sensor approach is investigated first in the paper. Then, the same sensor elements used for the continuous sensor are connected in an $N$-by-$N$ array that causes the individual signals from the sensors to be combined into $2N-1$ array outputs, as compared to the single output from before. For large array sizes, this approach greatly reduces the number of channels of data acquisition instrumentation needed for structural health monitoring. A trade-off in these two approaches is that the continuous sensor is the simplest with only one channel of data acquisition, while the array uses more channels to more accurately locate damage. A method is presented for locating the source of an acoustic emission based upon the identification of the dominant lower frequency components of flexural wave mode from the voltage time histories measured by four different continuous sensors at the four sides of a glass–epoxy simply supported plate.

## WAVE PROPAGATION MODELING

The technique that is used to model wave propagation in a plate is discussed. A signal processing method that uses wavelets to identify waves that propagate with minimal dispersion is also discussed.

### Acoustic Emission Modeling

The following is the equation of motion for the simply supported quasi-isotropic glass epoxy composite plate under a step force load excitation. This is done to simulate lead break of a 0.3 mm mechanical pencil, which simulates the acoustic emission from a propagating damage.

$$D\nabla^4 w(x,y,t) = -\rho h\ddot{w} + \frac{F(x,y,t)}{ab} \tag{1}$$

where the step function force $F(x,y,t) = \overline{F}U(t)\delta(x-x_c)\delta(y-y_c)$ gives the magnitude of excitation, $w$ is the deflection, $\rho$ is the mass density, $h$ is the plate thickness, $a$ and $b$ are the plate length and width, and the plate flexural rigidity is given as $D = (Eh^3/12(1-\nu^2))$. The boundary conditions are: $w=0$, $(\partial^2 w/\partial x^2)=0$, at $x=0$, $x=a$, and $w=0$, $(\partial^2 w/\partial y^2)=0$, $y=0$, $y=b$. After applying the Navier solution and using the orthogonalization property for separation of the spatial and time variable, the temporal equation is obtained. After addition of modal damping where each damping ratio is specified independently, the temporal equation becomes:

$$\ddot{a}_{mn} + 2\zeta_{mn}\omega_{mn}\dot{a}_{mn} + \omega_{mn}^2 a_{mn} = (\overline{F_{mn}}) \tag{2}$$

where:

$$a_{mn} = \frac{\overline{F}_{mn}}{\omega_{mn}^2} - \left(\frac{\overline{F}_{mn}}{\omega_{mn}\omega_{d_{mn}}} \mathrm{e}^{-\zeta_{mn}\omega_{mn}t}\cos(\omega_{d_{mn}}t-\theta)\right) \tag{3}$$

when:

$$t>0, \quad \theta = \tan^{-1}\left(\frac{\varsigma}{\sqrt{1-\varsigma^2}}\right), \quad \omega_{d_{mn}} = \omega_{mn}\sqrt{1-\zeta_{mn}^2} \quad \text{and} \quad \omega_{mn} = \pi^2\sqrt{\frac{D}{\rho h}\left[\left(\frac{m}{a}\right)^2+\left(\frac{n}{b}\right)^2\right]}.$$

The total solution for the plate displacement is:

$$w(x,y,t) = \sum_n\sum_m \left(\frac{\overline{F}_{mn}}{\omega_{mn}^2} - \left(\frac{\overline{F}_{mn}}{\omega_{mn}\omega_{d_{mn}}} e^{-\zeta_{mn}\omega_{mn}t}\cos(\omega_{d_{mn}}t-\theta)\right)\right)\sin\left(\frac{m\pi x}{a}\right)\sin\left(\frac{n\pi y}{b}\right) \tag{4}$$

where:

$$\overline{F}_{mn} = \frac{4F_0U(t)}{\rho hab}\sin\left(\frac{m\pi x_c}{a}\right)\sin\left(\frac{n\pi y_c}{b}\right). \tag{5}$$

Here $U(t)=0$ when $t\leq 0$ and $U(t)=1$ when $t>0$. The source amplitude is taken normally as $F_0=1\,\mathrm{N}$ [19–22] but in the simulation cases that were ran it was taken as 0.75 N. The corresponding strains are:

$$\varepsilon_x(x,y,t)=-z\frac{\partial^2 w}{\partial x^2}=-z\sum_n\sum_m a_{mn}(t)\sin\frac{m\pi x}{a}\sin\frac{n\pi y}{b}\left(\frac{m\pi}{a}\right)^2 \tag{6}$$

$$\varepsilon_y(x,y,t)=-z\sum_n\sum_m a_{mn}(t)\sin\frac{m\pi x}{a}\sin\frac{n\pi y}{b}\left(\frac{n\pi}{b}\right)^2 \tag{7}$$

$$\gamma_{xy}(x,y,t)=2z\frac{\partial^2 w}{\partial x\partial y}=2z\sum_n\sum_m a_{mn}(t)\cos\frac{m\pi x}{a}\cos\frac{n\pi y}{b}\left(\frac{m\pi}{a}\right)\left(\frac{n\pi}{b}\right). \tag{8}$$

The average strains over the area of the sensor are used to compute the voltage output from the PZT sensors used in this work. For a simple approximation to model a unidirectional active fiber composite patch bonded to a plate, the open circuit output voltage can be approximated using the average strain over the sensor nodes as:

$$V_0=\frac{\bar{\varepsilon}he}{\varepsilon^s} \tag{9}$$

where $\bar{\varepsilon}$ is the average strain and $\varepsilon^s$ is the permittivity. The average strain in the $X$-direction is computed for the nodes as:

$$\overline{\varepsilon_x}(t)=-\frac{h}{2}\frac{1}{\Delta x\Delta y}\int_{y_1}^{y_2}\int_{x_1}^{x_2}\sum_n\sum_m\left(\frac{m\pi}{a}\right)^2 a_{mn}(t)\sin\frac{m\pi x}{a}\sin\frac{n\pi y}{b}\,\mathrm{d}x\,\mathrm{d}y. \tag{10}$$

Upon double integration the average strain in the $x$-direction is:

$$\overline{\varepsilon_x}(t)=-\frac{h}{2}\frac{1}{\Delta x\Delta y}\left(\sum_n\sum_m\frac{(m\pi/a)}{(n\pi/b)}\right)a_{mn}(t)\left(\cos\frac{m\pi x_2}{a}-\cos\frac{m\pi x_1}{a}\right)\left(\cos\frac{n\pi y_2}{b}-\cos\frac{n\pi y_1}{b}\right) \tag{11}$$

where $\Delta x=x_2-x_1$ and $\Delta y=y_2-y_1$. The strain in the $y$-direction is computed similarly. In the case of the bi-directional PZT, the sum of the strains in both directions gives the total strain, neglecting in-plane shear strains. In the simulation, the elastic solution is computed at small time steps. The solution approach presented assumes that the rate of change of the excitation is less than the speed of propagation of waves in the material. Using this solution, continuous sensor designs can be practically studied to sense AE signatures and wave propagation. Considering a monolithic, electroded piezoceramic material subjected to bi-directional strain, the following can be derived from PZT constitutive equations (Equations (18) and (19) stated later in the paper):

$$D_j=\varepsilon^S E_j(t)+\left(e_{31}\frac{\partial w(x_j,y_j,t)}{\partial x}+e_{32}\frac{\partial w(x_j,y_j,t)}{\partial y}\right)\mathrm{sgn}(j). \tag{12}$$

Corresponding to Equation (12), the current generated by the *j*th segment of the sensor is:

$$i_j = \dot{D}_j A_e = C_p \dot{V}_o + \left( e_{31} \frac{\partial^2 w(x_j, y_j, t)}{\partial x \partial t} + e_{32} \frac{\partial^2 w(x_j, y_j, t)}{\partial y \partial t} \right) A_e \text{sgn}(j) \tag{13}$$

where $j$ is used to represent the $j$th electroded section of the sensor, $t$ is time, $w(x_j, t)$ is the plate displacement at segment $j$, and the sgn function allows for the connection of the sensors in positive or negative polarities. The simply supported plate is modeled to study the benefits of various PZT sensor array configurations for measuring strain and acoustic emissions.

**Active Wave Propagation Modeling**

An analytical model has been created for active acoustic wave propagation in a plate due to surface bonded PZT patches. The closed form solution for wave propagation due to actuation by a PZT actuator is briefly stated here. From the classical theory of vibration of plates, the equation of motion has been derived in terms of internal plate flexural moments $M_x$, $M_{xy}$, and $M_y$, and actuator induced moments $m_x$ and $m_y$ and then expressed in displacement form as:

$$D\nabla^4 w(x, y, t) + \rho h \ddot{w} = \frac{\partial^2 m_x}{\partial x^2} + \frac{\partial^2 m_y}{\partial y^2}. \tag{14}$$

The moments induced by the actuator patch are expressed as Heaviside step functions.

$$\begin{aligned} m_x &= m_x^1 [H(x - x_1) - H(x - x_2)][H(y - y_1) - H(y - y_2)] f(t) \\ m_y &= m_y^1 [H(x - x_1) - H(x - x_2)][H(y - y_1) - H(y - y_2)] f(t) \end{aligned} \tag{15}$$

where $f(t)$ is purely a function of time and in this case of impulse moment is expressed as delta functions. The temporal equation is derived in terms of modes using separation of spatial and time variables, and orthogonal relationships of trigonometric functions. A similar procedure was followed in the lead break analysis solved for the plate displacements due to step excitation. For an impulse moment actuation the plate displacement is expressed in terms of a Fourier series (Navier's solution) and by summation of modes giving the following:

$$w(x, y, t) = \sum_n \sum_m \frac{\overline{F}_{mn}}{\omega_{d_{mn}}} e^{-\zeta_{mn}\omega_{mn}t} \sin(\omega_{d_{mn}} t) \sin\left(\frac{m\pi x}{a}\right) \sin\left(\frac{n\pi y}{b}\right) \tag{16}$$

where

$$\overline{F}_{mn} = \frac{4\Delta t}{\rho h a b}(-1)\left[ m_x^1 \frac{mb}{na} + m_y^2 \frac{na}{mb} \right] \left( \cos\frac{m\pi x_1}{a} - \cos\frac{m\pi x_2}{a} \right) \left( \cos\frac{m\pi y_1}{a} - \cos\frac{m\pi y_2}{a} \right). \tag{17}$$

The variables $a$ and $b$ are the width and length of the plate in $x$ and $y$ directions, $m$ and $n$ are the mode numbers, $h$ is the thickness of the plate, $m_x^1$ and $m_y^1$ are the distributed surface moments, $\rho$ is the mass density of the fiberglass plate, and $z$ is $h/2$. The corresponding

strains are computed from Equations (6)–(8). The variables $x_1$, $x_2$, $y_1$, and $y_2$ represent the boundaries or edges of the PZT element. The derivation of $m_x^1$ and $m_y^1$ requires certain assumptions which are stated as follows: (a) the PZT patch element is poled in the $z$-direction and experiences equal strains in the $x$- and $y$-directions when exposed to an electric field (this is true only if the strain coefficients $d_{31}$ and $d_{32}$ are equal which is assumed in this case); (b) the plate is assumed to be a rectangular simply supported isotropic plate; (c) the stress distribution within the plate is assumed to be symmetric about the neutral axis and the bending of the plate produces a linear normal stress distribution (this assumes that the neutral axis is coincident with the mid-plane of the plate, although in actuality this may not be true, it is a valid approximation because the mass and flexural rigidity of the PZT element are significantly less than that of the plate); (d) actuator stress can be integrated to obtain the equivalent bending moment; (e) the bond between the plate and the PZT element is assumed to be perfect; (f) the stress distribution through the thickness of the PZT element is assumed to have the same slope as the stress distribution through the thickness of the plate that it is bonded to. The unconstrained strains in the PZT element are given by the following where the subscript pzt denotes strain in the PZT element.

**Modeling the Sensor**

The piezoceramic sensor nodes can be modeled as a capacitor in parallel with a current source. The piezoelectric constitutive equations used are listed in the IEEE standard ANSI/IEEE Std. 176-1987. These equations can be put into matrix form to give:

$$\begin{bmatrix} D \\ T \end{bmatrix} = \begin{bmatrix} \varepsilon^S & e \\ -e_t & c^E \end{bmatrix} \cdot \begin{bmatrix} E \\ S \end{bmatrix} \quad \begin{bmatrix} D \\ S \end{bmatrix} = \begin{bmatrix} \varepsilon^T & d \\ d_t & s^E \end{bmatrix} \cdot \begin{bmatrix} E \\ T \end{bmatrix}. \tag{18, 19}$$

The piezoceramic sensors can be modeled using the piezoelectric constitutive equations and by connecting the segments into an electric circuit as shown in Figure 1. Please refer to Reference [12] for the full derivation, but the expression for the output voltage equation for a continuous sensor nerve using Kirchhoff's law is:

$$\frac{\mathrm{d}}{\mathrm{d}t}(i) + \frac{n \cdot i}{RC} = \frac{eA_e}{RC} \sum_{j=1}^{n} \dot{S}_j \tag{20}$$

where $C$ is the capacitance of the PZT sensor, the effective capacitor area is $A_e$, the effective plate separation distance is $h$, $i_c$ represents the component of the current going through the capacitor of the model, and $i_g$ represents the component of the current generated by the piezoelectric sensor. The homogeneous and particular solutions for Equation (20) must be calculated and added for the total solution of the current $i$. The product of the current $i(t)$, and the impedance $R$ of the measuring device equals the voltage of the series connected sensors as a function of time. Thus we solve for the current to get the voltage $V_0 = iR$. This voltage is proportional to the dynamic strain in the structure at the sensor and thus can be used to detect damage through dynamic strain measurements and acoustic emissions. The current is numerically computed using the implicit Newmark-beta time marching scheme. Figure 1(a) and (b) shows examples of a continuous sensor and a $3 \times 3$ cross sensor array architecture.

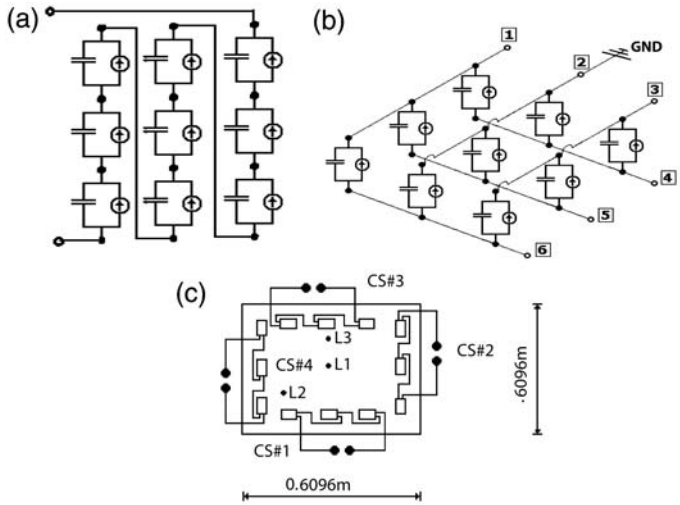


***Figure 1.*** *Circuit model of sensor (a) continuous sensor, (b) cross-sensor array, (c) a plate with four continuous sensors CS#1, CS#2, CS#3 and CS#4 along its four sides which is used in the passive modeling. L1, L2 and L3 are the points of three lead breaks for Case 1, Case 2 and Case 3.*

## Flexural Wave Propagation Velocity

Expressing the equation of motion (Equation 1) in polar co-ordinates and then by applying Hankel's transforms, the plate flexural wave number and the corresponding flexural wave velocity for a SS rectangular isotropic plate is derived as shown in Reference [27]. The flexural wave velocity is dispersive with higher frequencies traveling faster than the lower frequencies. It is given by

$$c_f = \sqrt[4]{\frac{D}{\rho h}}\sqrt{\omega} \tag{21}$$

where flexural stiffness of plate is given by $D = (Eh^3/12(1-\nu^2))$. In the present paper we are interested in identifying dominating lower frequency components of the flexural wave mode.

## Power Spectral Density and Wavelet Analysis

The FFT is done on the voltage-time history obtained from the continuous sensors which are surface bonded on the plate and then the power spectral density is plotted with respect to frequencies to identify the dominant flexural bandwidth and the peak frequency especially for the lower frequency components of the flexural mode. The wavelet analysis (scalogram) is then done to identify and narrow the time bandwidth considerably when the flexural wave with the peak amplitude hits one part of the continuous sensors. Below is a brief description of the wavelet analysis used to produce the scalograms. The continuous wavelet transform of $x(t)$ is a time-scale method of signal processing that is defined as:

$$W_\psi(a \cdot b) = \frac{1}{\sqrt{a}} \int_{-\infty}^{+\infty} x(t) \Psi^* \left( \frac{t-b}{a} \right) \mathrm{d}t. \tag{22}$$

In Equation (22), $b$ is a translation indicating the locality, $a$ is a dilation or scale parameter, $\Psi(t)$ is an analyzing wavelet, and $\Psi^*(t)$ is the complex conjugate of $\Psi(t)$. The scale parameter $a$ determines the frequency localization. The analyzing wavelet $\Psi(t)$ must satisfy the admissibility condition:

$$C_\psi = \int_{-\infty}^{+\infty} \frac{|\Psi(f)|^2}{|f|} \mathrm{d}f < \infty \tag{23}$$

where $\Psi(f)$ is the Fourier transform of $\Psi(t)$. This condition is required for obtaining the inverse of the wavelet transform. The Morlet wavelet is defined as:

$$\Psi(t) = e^{j2\pi f_0 t} e^{-(|t|^2/2)}, \quad \Psi(f) = \sqrt{2}\pi e^{-2\pi^2 (f-f_0)^2} \tag{24}$$

The Morlet wavelet gives a good dilation and translation selectivity. In practice the value of $f_0 > 5$ is used which meets approximately the requirements given by Equation (22). It is clear from the definition that the Fourier transform extracts periodic infinite waves from the analyzed function. In contrast, the wavelet transform analyses a function only locally at windows defined by a mother wavelet. Equation (24) is in general non-local. The value of $W_g(a, b)$ at a point $(a_0, b_0)$ depends on $x(t)$ $\forall t$. However from conditions of the wavelet, the function $\Psi(t)$ decays to zero at $-\infty$ and $+\infty$. If one assumes a fast decay, i.e. the values of $\Psi(t)$ are negligible outside the interval $(t_{\min}, t_{\max})$, the transform becomes local. The frequency localization is clear when the wavelet transform is expressed in terms of the Fourier transform:

$$W_\psi(a, b) = \sqrt{a} \int_{-\infty}^{+\infty} X(f) \Psi^*_{a,b}(af) e^{i2\pi f b} \mathrm{d}f \tag{25}$$

where the localization depends on the dilation (scale) parameter $a$. The local resolution of the wavelet transform in time and frequency is determined by the duration and bandwidth of the analyzing functions given by $\Delta t = a\Delta t_g$ and $\Delta f = \Delta f_g / a$, where $\Delta t_g$ and $\Delta f_g$ are the duration and the bandwidth of the basic wavelet function, respectively. Thus, in the frequency domain, the wavelet transform has good resolution at low frequencies and in the time domain at high frequencies. The latter is more suitable for transient signal detection. The wavelet transform as a signal decomposition tool cannot be directly compared to any time–frequency representation. However there is a relationship between dilation and frequency. For the Morlet analyzing wavelet, the relationship between the dilation parameter $a_f$ and the signal frequency $f_x$ is given by:

$$a_f = f_0 \frac{f_s}{f_w} \frac{1}{f_x} \tag{26}$$

where $f_s$ is the signal sampling frequency and $f_w$ is the wavelet sampling frequency.

In the present article, the time bandwidth is very large in order to capture the dominant lower frequency components of the flexural wave mode. This results into bandwidth resolution problems when trying to generate a scalogram (frequency vs. time wavelet map) as there is a minimum area rule for wavelet analysis for frequency vs. time measurements.

Hence it becomes harder to find the initial time with greater accuracy than done in this article when a particular frequency or frequency bandwidth starts to be present in the voltage time history graph when such wavelet time-frequency maps are used. It is expected that plotting the amplitude–time trace of the frequency component of interest might show the arrival time more clearly.

## SIMULATION OF WAVE PROPAGATION

Active wave propagation and passive sensing of acoustic waves can be done using the distributed sensor. These two approaches to damage detection are considered in this section.

### Active Wave Generation and Sensing

The simulation is performed using a model of the glass–epoxy composite plate. One case of active wave propagation using a surface bonded PZT actuator located at the center of the rectangular SS plate and sensing using continuous and array sensors is presented here. The material properties of the glass–epoxy plate can be found in Reference [11]. The size of the plate is $0.88\,\text{m} \times 1.21\,\text{m} \times 3.2\,\text{mm}$. The first 100 vibration modes have been used for the simulation and the time step used is $1\,\mu\text{s}$. Figure 1(a) shows the continuous sensor and Figure 1(b) shows the cross array sensor architecture which have been used here. Figure 2 shows the active wave propagation at the times 10–360 μs due to the anti-symmetric Lamb waves (flexural waves) generated by a PZT actuator placed at the center of the glass–epoxy plate. The actuator dimensions are $2.5\,\text{cm} \times 5\,\text{cm} \times 0.25\,\text{mm}$. Figures 3 and 4 shows the voltage–time history of the array sensors and the continuous sensors modeled on the plate.

***Figure 2.*** *Wave propagation at 10, 60, 110, 160, 210, 260, 310, and 360 $\mu$m due to center actuation by a PZT patch.*

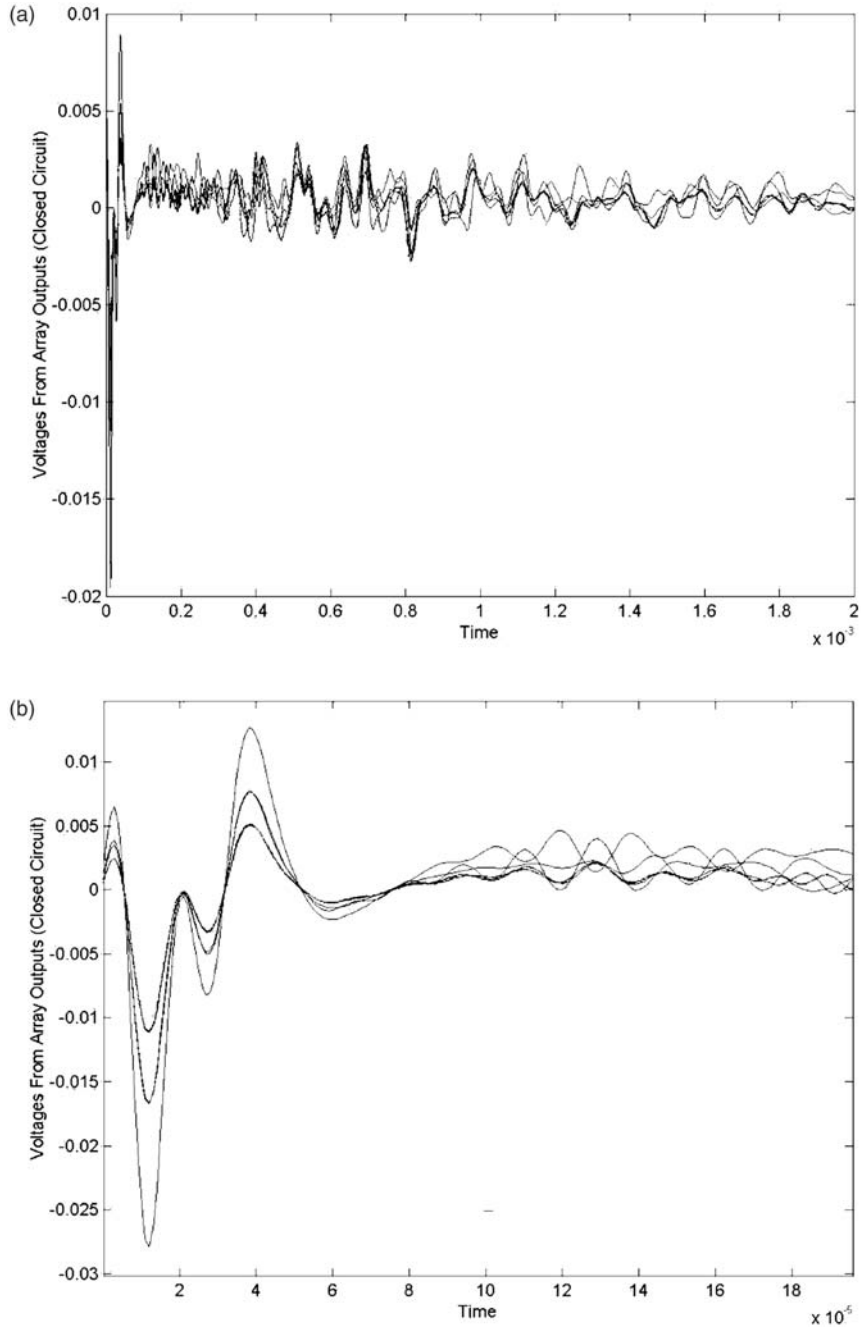


***Figure 3.*** *Voltage time history due to center actuation by a PZT patch: (a) array voltage for 2 ms and (b) array voltage for 0.2 ms.*

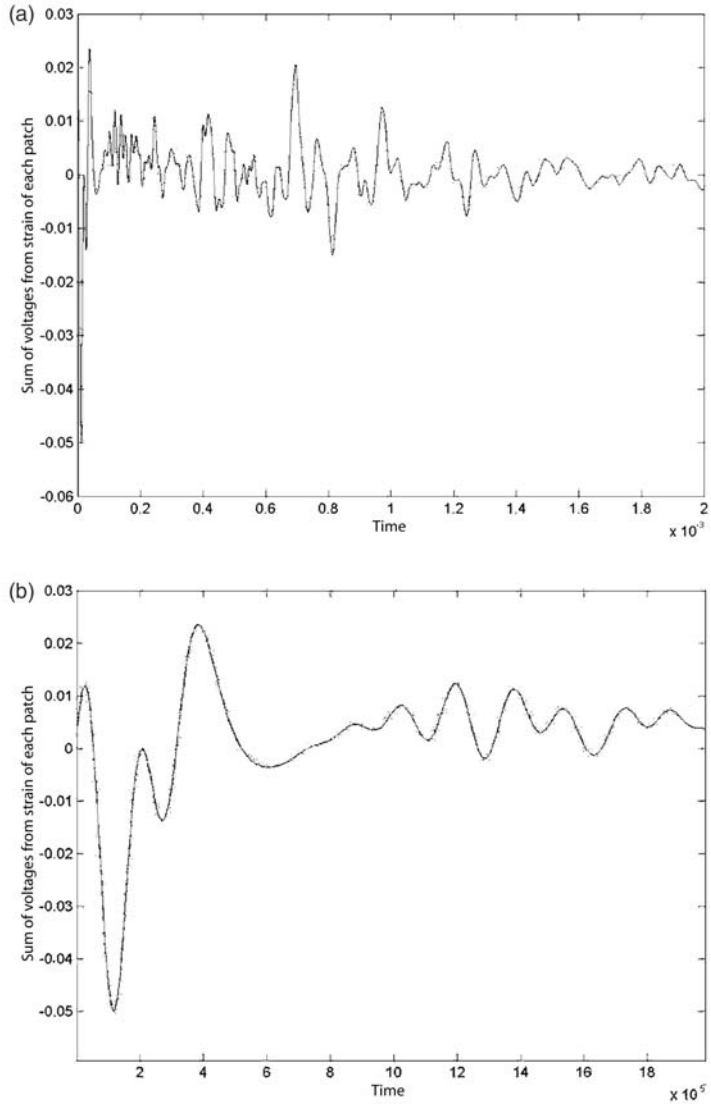


***Figure 4.*** *Voltage time history due to center actuation by a PZT patch: (a) continuous sensor voltage for 2 ms and (b) continuous sensor voltage for 0.2 ms.*

## Passive Wave Generation and Damage Location using Continuous Sensors

Figures 5–7 and Table 1 represent three cases of lead break analysis on a glass epoxy plate (same material property as the above plate) of $0.6096\,\text{m} \times 0.6096\,\text{m} \times 3.2\,\text{mm}$ dimensions. Lead break signals from a 0.3 mm mechanical pencil simulate the acoustic emission from the micro-fiber breaking at three different locations on the plate as shown in Figure 1(c). Figure 1(c) gives the placement of CS#1, CS#2, CS#3, and CS#4 on the plate. L1, L2, and L3 are the locations of lead breaks for Case 1, Case 2, and Case 3. Table 1 gives the placement details of the continuous sensors. CS#1 consists of sensors 1, 2, and 3, CS#2 consists of sensors 4, 5, and 6, CS#3 consists of sensors 7, 8, and 9 and CS#4 consists

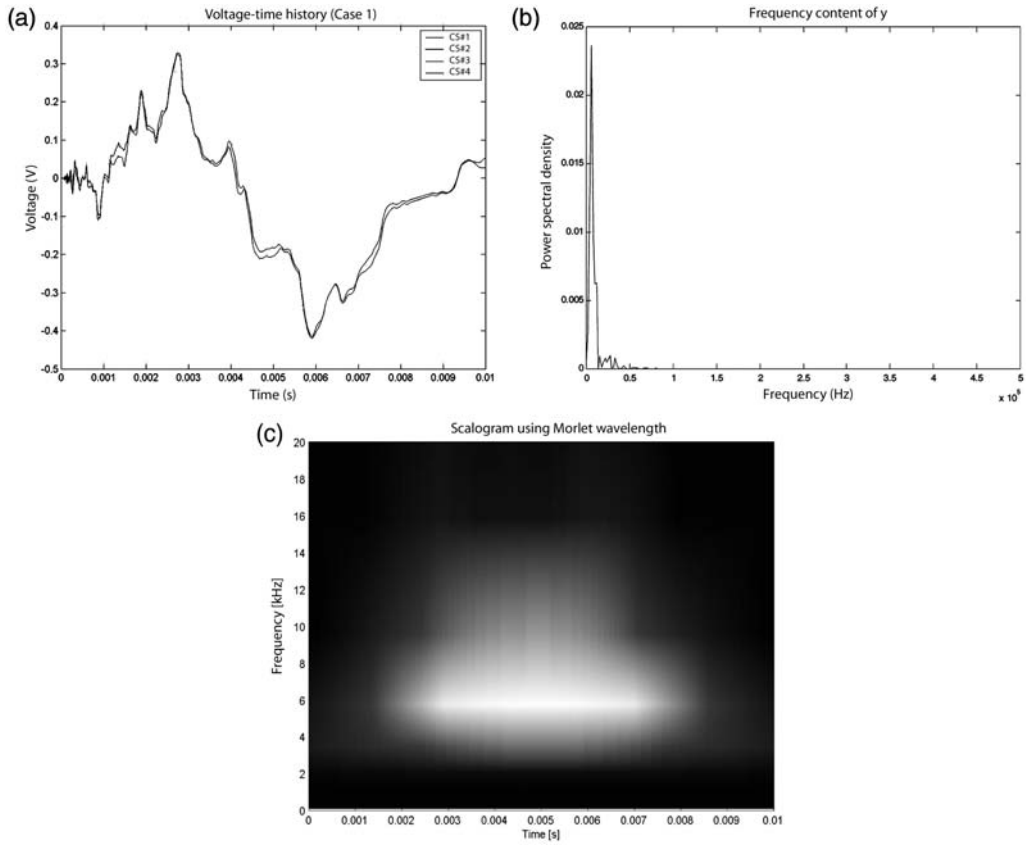


***Figure 5.*** *Case 1 (a) represents the voltage–time histories of CS#1, CS#2, CS#3 and CS#4. (b) Shows the power spectral density vs. frequency for CS#1 to find the dominant lower frequency component of the flexural mode in CS#1. The frequency is this case is 5958.375 Hz. (c) Case 1 scalogram using the Morlet wavelet to capture the frequency vs. time to get an estimated time at which the dominant frequency*

of sensors 10, 11, and 12. All co-ordinates are given in inches in this table (needs to be divided by 39.37 to be converted to meters).

The methodology followed for localizing the simulated damage position is as follows. The voltage time histories for four different continuous sensors located at the four sides of the plate were measured separately. Each continuous sensor consists of three pzt sensors of are 2.5 cm × 5 cm × 0.25 mm dimensions connected serially to give one output. The power spectral density and the frequency plots are done to identify the dominant lower frequency components of the flexural wave mode (which signifies the major energy contributor to the system) and the associated peak frequency. A wavelet scalogram is performed to narrow down the initial time when the associated peak frequency might have reached the continuous sensors. By returning to the original voltage time history graph, the time when the peak flexural wave reaches the continuous sensor is estimated. The corresponding velocity of the flexural wave propagation for the peak frequency is then computed. Thus, the $x$ or $y$ co-ordinate distance, depending on the orientation of the continuous sensors i.e. on the sides of the plate where they are located, of the simulated damage location from the continuous sensors is computed and then the error is estimated as shown in Table 2.

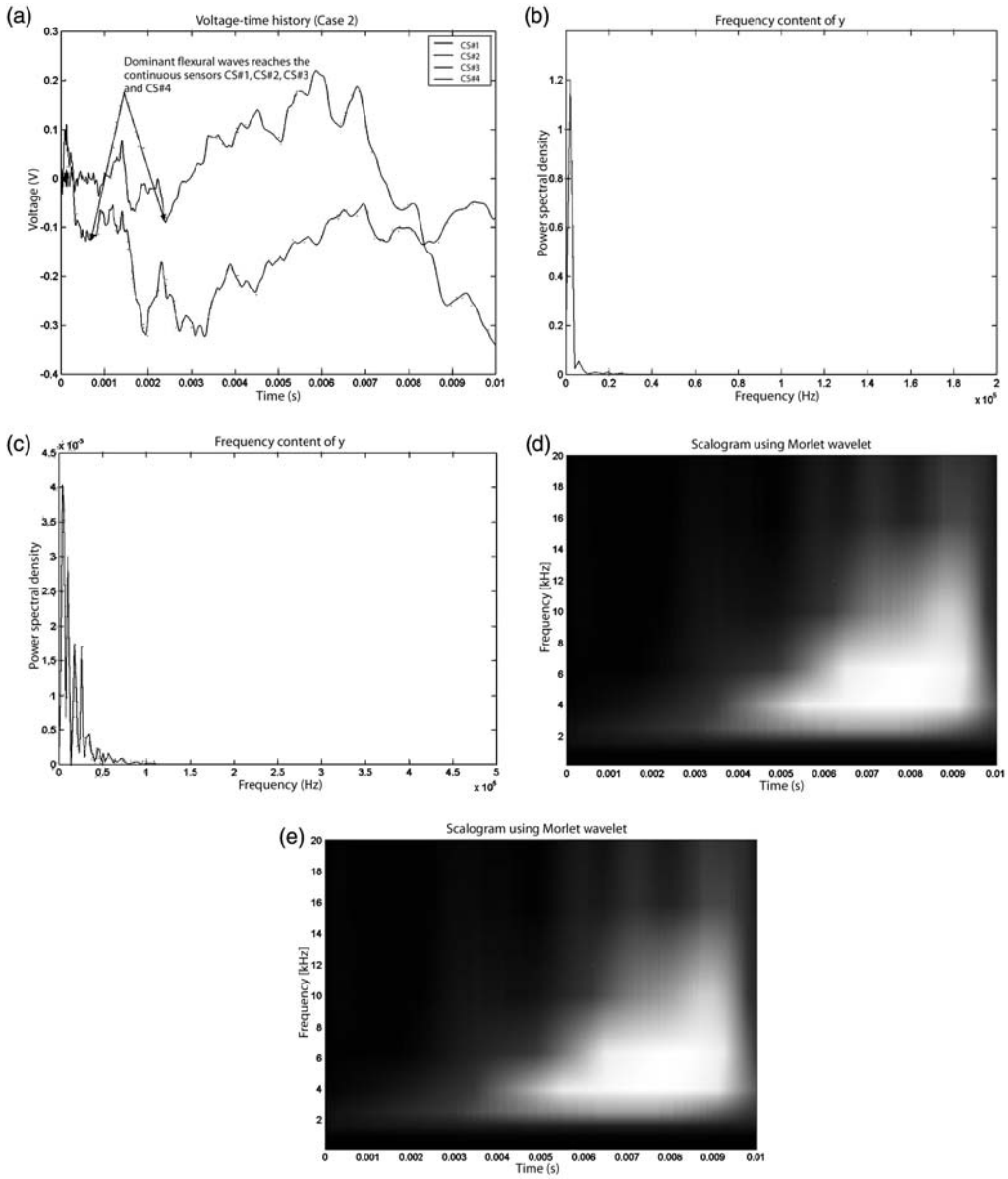


***Figure 6.*** *Case 2 (a) represents the voltage–time histories of CS#1, CS#2, CS#3, and CS#4 and the estimated time when the dominant flexural waves reach the respective continuous sensors. (b) Case 2 shows the power spectral density vs. frequency for CS#1 to find the dominating flexural frequency in CS#1. The frequency is this case is 1953.12 Hz. (c) Case 2 shows the power spectral density vs. frequency for CS#1 to find the dominating flexural frequency in CS#2. The frequency is this case is 3906.25 Hz. (d) Case 2 scalogram using Morlet wavelet to capture the frequency vs. time to get an estimated time at which the dominant frequency reaches CS#2. (e) Case 2 scalogram using Morlet wavelet to capture the frequency vs. time to get an estimated time at which the dominant frequency reaches CS#3.*

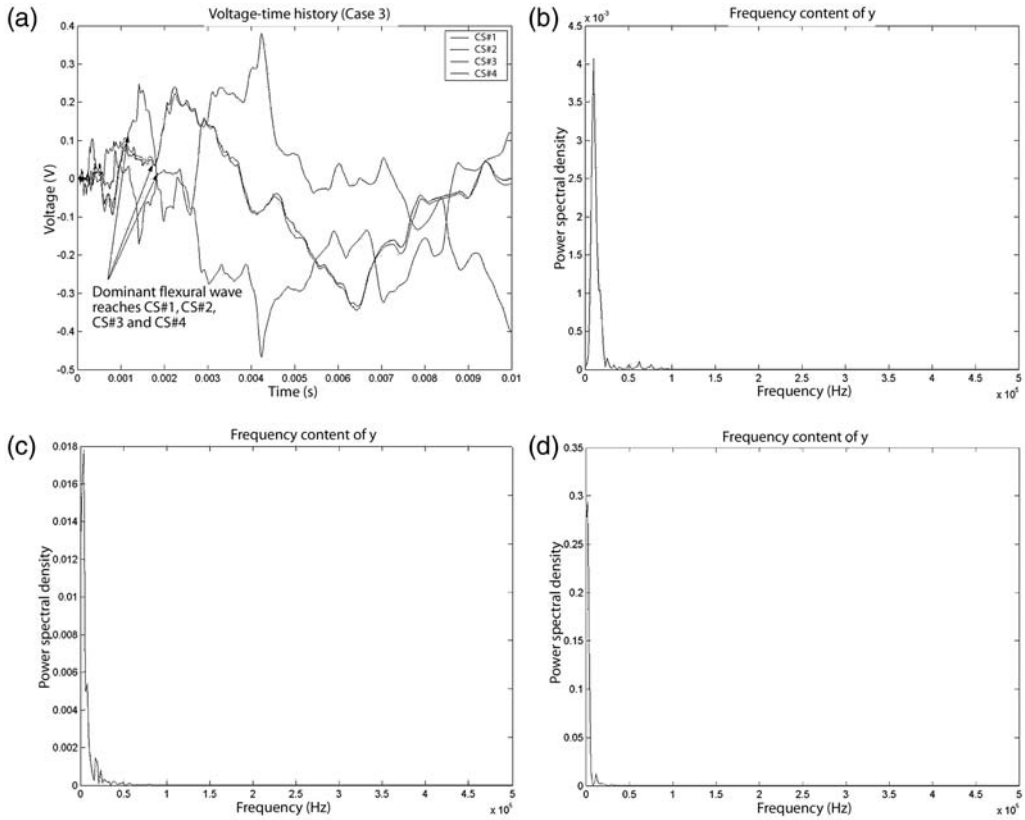


***Figure 7.*** *Case 3 (a) Voltage time histories for continuous sensors CS1, CS2, CS3, and CS4 and indicating the estimated time when the peak frequency reaches those sensors respectively. (b–d) PSD graphs for CS#1, CS#2, and CS#3. (e) Scalogram using Morlet wavelet to capture the frequency vs. time to get an estimated time at which the dominant frequency reaches CS#1. (f) Scalogram using Morlet wavelet to capture the frequency vs. time to get an estimated time at which the dominant frequency reaches CS#2. (g) Scalogram using Morlet wavelet to capture the frequency vs. time to get an estimated time at which the dominant*

Figure 5 represents Case 1 where (a) represents the voltage–time histories of continuous sensors CS#1, CS#2, CS#3, and CS#4. Figure 5(b) shows the power spectral density vs. frequency for CS#1 to find the dominant flexural frequency in CS#1. The frequency in this case is 5958.375 Hz. Figure 1(c) for Case 1 is the scalogram using the Morlet wavelet to capture the frequency vs. time to get an estimated time at which the dominant frequency reaches CS #1. Since the plate is square and the source is located at the center, the responses in this case are equal. Figure 6 represents Case 2 where Figure 6(a) shows the voltage–time histories of CS#1, CS#2, CS#3, and CS#4 and the estimated time when the dominant flexural waves reaches the respective continuous sensors. Figure 6(b) shows the power spectral density vs. frequency plots for CS#1 to determine the dominating flexural frequency in CS#1. The frequency is this case is 1953.12 Hz. Figure 6(c) shows the power spectral density vs. frequency plots for CS#2 to find the dominant flexural frequency in CS#2. The frequency is this case is 3906.25 Hz. Figure 6(d) shows the scalogram using the Morlet wavelet to capture the frequency vs. time to get an estimated time period at which the dominant frequency reaches CS#2. Figure 6(e) represents the scalogram using the Morlet wavelet to capture the frequency vs. time to get an estimated

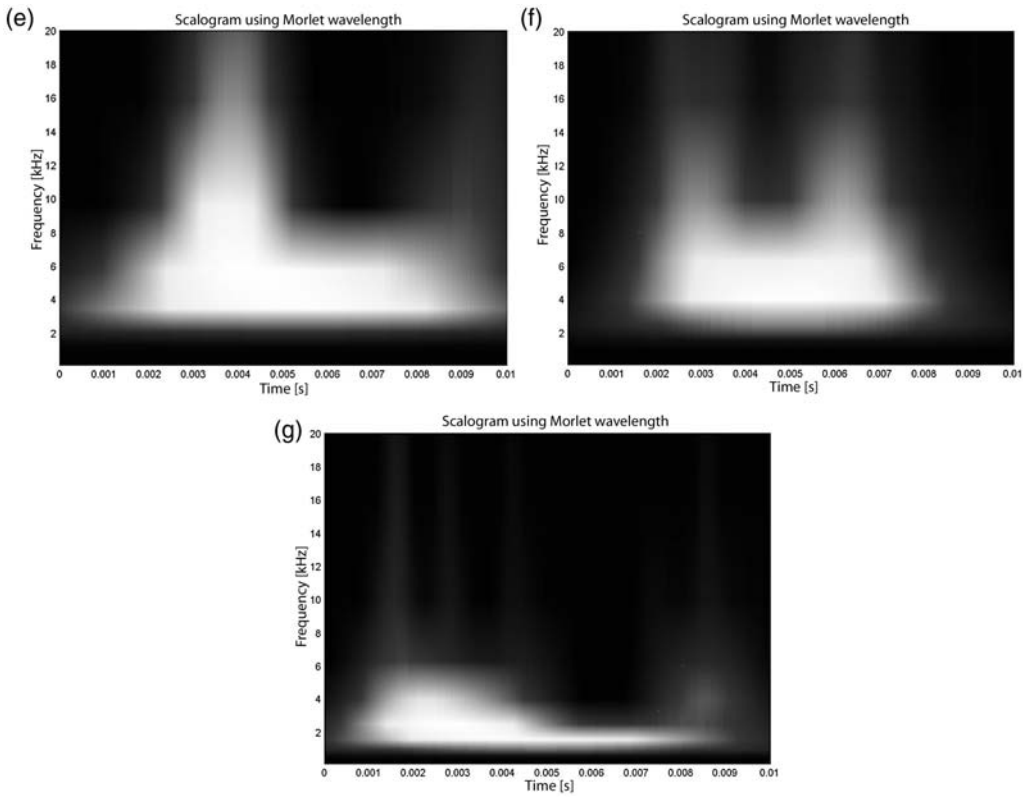


***Figure 7.*** *Continued.*

***Table 1. CS#1 consists of sensors 1, 2, and 3. CS#2 consists of sensors 4, 5, and 6. CS#3 consists of sensors 7, 8, and 9. CS#4 consists of sensors 10, 11, and 12. All co-ordinates are given in inches (needs to be divided by 39.37 to be converted to m).***

| Continuous sensor | Sensor | X1 | X2 | Y1 | Y2 |
|---|---|---|---|---|---|
| | 1 | 5.75 | 6.25 | 4.0 | 4.25 |
| CS#1 | 2 | 11.75 | 12.25 | 4.0 | 4.25 |
| | 3 | 17.75 | 18.25 | 4.0 | 4.25 |
| | 4 | 20.0 | 20.25 | 5.75 | 6.25 |
| CS#2 | 5 | 20.0 | 20.25 | 11.75 | 12.25 |
| | 6 | 20.0 | 20.25 | 17.75 | 18.25 |
| | 7 | 5.75 | 6.25 | 20.0 | 20.25 |
| CS#3 | 8 | 11.75 | 12.25 | 20.0 | 20.25 |
| | 9 | 17.75 | 18.25 | 20.0 | 20.25 |
| | 10 | 4.0 | 4.25 | 17.75 | 18.25 |
| CS#4 | 11 | 4.0 | 4.25 | 11.75 | 12.25 |
| | 12 | 4.0 | 4.25 | 5.75 | 6.25 |

***Table 2. Details of the actual/computed location of the damage and the error associated. It shows the values of the peak frequencies and the associated velocity of propagation.***

| | Case #1 | Case #2 | Case #3 |
|---|---|---|---|
| Damage position X | 12 in/0.3048 m | 6 in/0.1524 m | 12 in/0.3048 m |
| Damage position Y | 12 in/0.3048 | 6 in/0.1524 m | 16 in/0.4064 m |
| CS1 dominant flexural freq/time at which it reaches CS1 | 5859.37 Hz/1.45e-03 s | 1953.12 Hz/5e-4 s | 9765.63 Hz/1.7e-03 s |
| CS2 dominant flexural freq/time at which it reaches CS2 | 5859.45 Hz/1.49e-03 s | 3906.25 Hz/2.85e-03 s | 3906.25 Hz/1.78e-03 s |
| CS3 dominant flexural freq/time at which it reaches CS3 | 5859.375 Hz/1.48e-03 s | 3906.25 Hz/2.8e-03 s | 1953.12 Hz/1.1e-03 s |
| CS4 dominant flexural freq/time at which it reaches CS4 | 5859.375 Hz/1.45e-03 s | 1953.12 Hz/5.7e-04 s | 3906.25 Hz/1.78e-03 s |
| Computed/actual damage Y-coord. dist from CS1. | 0.2076 m/0.1969 m | 0.04163 m/0.0445 m | 0.3142 m/0.2985 m |
| Computed/actual damage X-coord. dist from CS2 | 0.2133 m/0.2032 m | 0.3331 m/0.3556 m | 0.2080 m/0.2032 m |
| Computed/actual damage Y-coord. dist from CS3. | 0.2126 m/0.2032 m | 0.3273 m/0.3556 m | 0.0909 m/0.1016 m |
| Computed/actual damage X-coord. dist from CS4. | 0.2112 m/0.1969 m | 0.0471 m/0.0445 m | 0.2080 m/0.1969 m |
| Error % in CS1 | 5.43% | 4.16% | 6.86% |
| Error % in CS2 | 4.97% | 6.33% | 2.36% |
| Error % in CS3 | 4.63% | 7.96% | 10.52% |
| Error % in CS4 | 7.26% | 5.52% | 5.64% |

Error % = {(computed value − actual value)/actual value} × 100.

time period at which the dominant frequency reaches CS#3. The actual time is further narrowed after going back to original voltage–time history graphs (Figure 6(a)). Figure 7 represents the Case 3 where Figure 7(a) is the voltage–time histories for continuous sensors CS1 CS2, CS3 and CS4, indicating the estimated time when the peak frequency reaches those sensors respectively. Figure 7(b–d) show the PSD graphs for CS#1, CS#2 and CS#3 to find the peak frequency and the dominant frequency bandwidth. Figure 7(e) is the scalogram using the Morlet wavelet to capture the frequency vs. time to get an estimated time at which the dominant frequency reaches CS#1. Figure 7(f) shows the scalogram using Morlet wavelet to capture the frequency vs. time to get an estimated time at which the dominant frequency reaches CS#2. Figure 7(g) is the scalogram using the Morlet wavelet to capture the frequency vs. time to get an estimated time at which the dominant frequency reaches CS#3. Table 2 shows the details of the actual/computed location of the damage and the error associated. It shows the values of the peak frequencies and the associated velocity of propagation for the flexural wave. The error percentages for the location co-ordinates of the simulated damage acoustic emission source (lead break) from computed to actual co-ordinates vary from 4% to 10% depending upon the case and the continuous sensors.

## CONCLUSIONS

The simulations for both active wave generation and passive sensing performed have shown that multiple piezoceramic patches can be connected together in a series or array

pattern to simulate the way biological nerves have multiple inputs (dendrites) connected together. This reduces the number of channels of data acquisition needed to detect damage represented by acoustic emissions or high strains. The simulation model developed can be used to optimize the design of the neural system for different structural materials and sizes. This can be used for simulating active interrogation for damage detection in plate type structures. The model is a useful tool for optimizing the actuator and sensor locations for both the continuous sensor nodes and for the sensor array configurations. The model is being used for devising a neural network algorithm for detection, localization, and quantification of the crack/damage and monitoring the survivability of the plate structure. It also shows that flexural wave analysis holds great promise for finding the damage location from acoustic emissions from passive continuous sensors. However the error in finding the initial time at which the predominant flexural wave reaches the sensor needs to be reduced. It is expected that plotting the amplitude–time trace of the frequency component of interest might show the arrival time more clearly. Currently efforts are underway to model a crack in the plate and use the actuator and sensor bonded on the plate to detect the crack. Further investigations are being done to correlate the peaks in the voltage time history graphs with the time when the incident and the reflected waves hit the sensors, and when the waves are scattered from a damage embedded in the plate. Also the flexural wave velocity of propagation analysis for locating the damage needs further simulation testing especially with experimental verification.

## REFERENCES


1. Pierce, S. G., Culshaw, B., Manson, G., Worden, K. and Staszewski, W. J. (2000). The Application of Ultrasonic Lamb Wave Techniques to the Evaluation of Advanced Composite Structures, *Proc. of SPIE*, **3986**: 93–103.
2. Allyne, D. N. and Cawley P. (1992). Optimization of Lamb Wave Inspection Techniques, *J. Destructive Testing and Evaluation International*, **25**(1): 11–22.
3. Pierce, S. G., Philp, W. R., Culshaw, B., Gachagan A., McNab, A., Hayward G. and Lecuyer, F. (1996). Surface-bonded Optical Sensors for the Inspection of CFRP Plates Using Utlrasonic Lamb Waves, *Smart Materials and Structures*, **5**: 776–787.
4. Gachagan, A., Hayward, G., McNab, A., Reynolds, P., Pierce, S. G., Philp, W. R. and Culshaw, B. (1999). Generation and Reception of Ultrasonic Guided Waves in Composite Plates Using Conformable Piezoelectric Transmitters and Optical-Fiber Detectors, *IEEE Trans. on Ultrasonics, Ferroelectrics, and Frequency Control*, **46**(1): 72–81.
5. Rose, J. L. (2000). Guided Wave Nuances for Ultrasonic Nondestructive Evaluation, *IEEE Trans. on Ultrasonics, Ferroelectrics, and Frequency Control*, **47**(3): 575–582.
6. Wang, C. and Chang, F. (2000). Diagnosis of Impact Damage in Composite Structures with Built-in Piezoelectrics Network, *Proceedings of the SPIE*, **3990**: 13.
7. Schwartz, W. G., Read, M. E., Kremer, M. J., Hinders, M. K. and Smith, B. T. (1999). Lamb Wave Tomographic Imaging System for Aircraft Structural Health Assessment, *SPIE Conference on NDE of Aging Aircraft, Airports, and Aerospace Hardware III*, Vol. 3586, p. 292, Newport Beach, CA.
8. Sundaresan, M. J., Ghoshal, A., Schulz, M. J. and Wilkerson, C. (2000). *Acoustic Emission Monitoring using Distributed Sensors,* ASNT Spring Conference and 9th Annual Research Symposium, Birmingham, Alablama, March 27–31.
9. Sundaresan, M. J., Schulz, M. J., Ghoshal, A. and Pratap, P. (2001). A Neural System for Structural Health Monitoring, *SPIE 8th Int. Symposium on Smart Materials and Structures*, Newport Beach, CA, March 4–8.
10. Sundaresan, M. J., Ghoshal, A. and Schulz, M. J. *Sensor Array System*, Patent Application, 6/00.
11. Ghoshal, A., Sundaresan, M. J., Schulz, M. J. and Pai, P. F. (2000). Continuous Sensors for Structural Health Monitoring, *Adaptive Structures and Material Systems Symposium at the International Mechanical Engineering Congress and Exposition Winter Annual Meeting of the ASME*, Nov. 5–10, Walt Disney World Dolphin, Orlando, FL.

12. Schulz, M. J., Sundaresan, M. J., Ghoshal, A. and Martin, W. N. (2001). Evaluation of Distributed Sensors for Structural Health Monitoring, *ASME DTEC'01 Conf*., Sept. 9–12, Pittsburgh, PA.
13. Doyle, J. F. (1997). *Wave Propagation in Structures*, **2nd edn**, Springer-Verlag, New York.
14. Achenbach, J. D. (1973). *Wave Propagation in Elastic Solids*, North Holland Publishing Company, New York.
15. Ballentine, D. S., White, R. M., Martin, S. J., Ricco, A. J., Zellers, E. T., Frye, G. C. and Wohltjen, H. (1997). *Acoustic Wave Sensors, Theory, Design and Physico-Chemical Applications*, Academic Press Inc., San Diego.
16. Campbell, C. K. (1998). *Surface Acoustic Wave Devices for Mobile and Wireless Communications*, Academic Press, San Diego.
17. Schmerr, L. W. Jr. (1998). *Fundamentals of Ultrasonic Nondestructive Evaluation*, Plenum Press, New York.
18. Wasley, R. J. (1973). *Stress Wave Propagation in Solids*, Marcel Dekker, Inc., New York.
19. Gorman, M. R. and Prosser, W. H. (1996). Application of Normal Mode Expansion to AE waves in Finite Plates, NASA Langley WebServer, *J. Appl. Mech*., **63**(2): 555–557.
20. Prosser, W. H. (1991). The Propagation Characteristics of the Plate Modes of Acoustic Emission Waves in thin Aluminum Plates and Thin Graphite/Epoxy Composites Plates and Tubes, PhD Dissertation, Johns Hopkins University, Baltimore, Maryland.
21. Hamstad, M. A., Gary, J. and O'Gallagher, A. (1996). Far Field Acoustic Emission Waves by Three Dimensional Finite Element Modeling of Pencil-Lead Breaks on a Thick Plate, *Journal of Acoustic Emission*, **14**(2): 103–114.
22. Johnson, M. and Gudmundson, P. (2001). Experimental and Theoretical Characterization of Acoustic Emission Transients in Composites Laminates, *Composites Science and Technology*, **61**: 1367–1378.
23. Dimitriadis, E. K., Fuller, C. R. and Rogers, C. A. (1991). Piezoelectric Actuators for Distributed Vibration Excitation of Thin Plates, *ASME Journal of Vibration and Acoustics*, **113**: 100–107.
24. Sonti, V. R., Kim, S. J. and Jones, J. D. (1995). Equivalent Forces and Wavenumber Spectra of Shaped Piezoelectric Actuators, *Journal of Sound and Vibration*, **187**(1): 111–131.
25. Lee, C. K. (1990). Theory of Laminated Piezoelectric Plates for the Design of Distributed Sensors/Actuators. Part I: Governing Equations and Reciprocal Relationships, *Journal of Acoustical Society of America*, **87**(3): 1144–1158.
26. Chee, C. Y. K., Tong, L. and Steven, G. (1998). A Review on the Modeling of Piezoelectric Sensors and Actuators Incorporated in Intelligent Structures, *Journal of Intelligent Materials and Structures*, Vol. 9, January. Technomic Publishing Co., Inc., Lancaster, PA 17604.
27. Junger, M. C. and Feit, D. (1993). *Sound, Structures and Their Interaction*, Acoustical Society of America, Cambridge, Mass.